

Implicit Large-Eddy Simulations of Hot and Cold Supersonic Jets in Loci-CHEM

C. I. Morris*

NASA Marshall Space Flight Center, Huntsville, AL, 35812, USA

E. A. Luke†

Mississippi State University, MS, 39762, USA

Submitted to the AIAA SciTech 2020 Forum, January 6–10, 2020, Orlando, FL

I. Abstract

TURBULENCE is a critical factor in most aero- and propulsion-related flows. For many years, the industry-standard approach to incorporating the effect of turbulence in computational fluid dynamics (CFD) calculations has been the Reynolds Averaged Navier Stokes (RANS) modeling approach. RANS implicitly time-averages turbulent motion, and models its effect on the mixing of species, momentum and energy in a flow field. The approach is economical and often allows a CFD calculation to proceed to steady-state. However, it makes several simplifying assumptions, and the results will only be as good as the RANS turbulence model. Meanwhile, the last two decades have witnessed rapid and explosive growth in computational power, the development of CFD codes which scale well over thousands of processors, and the refinement of unstructured grid-generation tools which facilitate rapid surface and volume gridding of complex geometries. CFD engineering calculations of $10^8 - 10^9$ finite-volume cells have become routine. Thus, large eddy simulation (LES), which attempts to directly resolve the unsteady motion of the largest scales of turbulence, is increasingly of interest for many fluids engineering problems.¹⁻³ Additionally, hybrid RANS-LES approaches such as Spalart's Detached Eddy Simulation (DES),⁴ which attempt to marry the best strengths of both methods, are in active use and development. Because it seeks to accurately resolve the unsteady motion of the largest scales of turbulence, LES places certain requirements on the numerical method used to discretize and advance the Navier Stokes equations. In particular, LES requires high time accuracy and minimal intrinsic numerical dispersion and dissipation over a wide range of length scales.

A round turbulent jet is an example of a foundational free shear turbulence problem that has been challenging for many RANS turbulence models. A rocket plume typically adds the complexity of compressibility and high jet temperature to the problem, and potentially the complication of plume expansion or shock waves when the plume is significantly under- or over-expanded with respect to the ambient environment. For solid rocket motors, particles can become a notable fraction of the exhaust mass, momentum and energy flow, and can exchange momentum and energy with the gas phase. These plumes are typically a significant driver of acoustic and thermal design environments and loads in the base region of a launch vehicle, and even more so for any surface directly impinged by the plume (e.g. a mobile launch platform). These plume-induced acoustic and thermal environments, and any impingement loads or heating, are strongly influenced by the turbulent mixing of rocket plumes with the ambient environment. Thus it is important to model or capture this mixing correctly. LES has shown promise for this goal.⁵⁻¹⁰

Here, both RANS and LES approaches are applied to modeling hot and cold supersonic turbulent jets. The basis of validation and comparison is the experimental work of Seiner et al.¹¹ In that paper, a nearly perfectly expanded jet with an exit Mach number of 2.0 was exhausted into a quiescent ambient environment at

*Aerothermodynamics Team Lead, Aerosciences Branch/EV33, Senior Member AIAA.

†Assistant Professor, Department of Computer Science and Engineering, Mississippi State University.

the Jet Noise Laboratory at NASA Langley. The jet exit diameter, D was 3.6 inches. A wide range of jet total temperatures were investigated, ranging from 313 K to 1534 K. In this work, two of these cases are considered: a cold jet with a total temperature of 313 K, and a hot jet with a total temperature of 1114 K. The jet exit Reynolds numbers, based on exit diameter and centerline flow properties, are 8.15×10^6 and 1.64×10^6 , respectively. Jet spreading rate data and near-field acoustic data for the comparisons below were obtained by digitizing Figures 8 and 18 in Reference 11. Axial profiles of Mach number, total temperature and total pressure for the comparisons below were obtained from the Axisymmetric Cold and Hot Supersonic Jet cases at the NASA Langley Turbulence Modeling Resource (https://turbmodels.larc.nasa.gov/jetsupersoniccold_val.html¹² and https://turbmodels.larc.nasa.gov/jetsupersonichot_val.html¹³). The website authors note that the data were obtained independently of Reference 11.

The CFD analysis was performed using the Loci-CHEM CFD code, version 4.0-beta-11_p1 (Reference 14). Loci-CHEM is a finite-volume flow solver for generalized grids developed at Mississippi State University in part through NASA and NSF funded efforts. Loci-CHEM is comprised entirely of C and C++ code and is supported on all popular UNIX variants and compilers. Efficient parallel operation is facilitated by the Loci¹⁵ framework which exploits multi-threaded and MPI libraries. The code supports the use of multi-species finite-rate chemistry models, and has several different RANS turbulence modeling options. It is widely used in NASA, the Department of Defense and Industry for CFD analysis of aerospace problems. Second-order spatial accuracy on unstructured grids is typically obtained by using a least-squares gradient reconstruction combined with a Barth¹⁶ or Venkatakrishnan-style¹⁷ limiter for compressible flow problems. The inviscid flux function is typically the Roe approximate Riemann solver.¹⁸ This baseline approach is denoted LS-Roe below. However, due to recent development work supported by the Space Launch System Program, Loci-CHEM can now also use an Optimized Gradient Reconstruction (OGRE)¹⁹ with the Roe flux (denoted OGRE-Roe below). This reconstruction also makes use of the method proposed by Thornber^{20,21} to reduce dissipation for subsonic flows. Further, a low-dissipation skew-symmetric central difference scheme which is fourth-order accurate on uniform meshes (denoted LDS4 below) was also developed for Loci-CHEM. A user-selectable amount of third-order upwinding can be blended into this scheme for stability and robustness—as little as 10% is effective. Both the OGRE-Roe flux and the low-dissipation flux (and particularly the latter) significantly improve the dispersion and dissipation characteristics of the inviscid flux calculation in Loci-CHEM compared to the baseline least-squares approach with the Roe flux. It should be noted that, at the present time, the low-dissipation central difference scheme functions more effectively on hexahedral or polyhedral meshes than tetrahedral meshes.

Four grids were used to help assess the dependence of solution accuracy on grid resolution. The boundaries of the solution domain are based on the grids available at Refs. 12 and 13. The converging-diverging nozzle is modeled, and the solution domain extends 1.205 jet exit diameters upstream from the nozzle exit, 36.67 diameters downstream, and 11.11 diameters radially from the jet centerline. Although Loci-CHEM is an inherently unstructured flow solver, the grid is largely based on a cylindrical structured grid approach. Grids with circumferential spacings of 3.0, 2.0, 1.5 and 1.0 degrees were developed for this study. The grid is also “bufferflied” to keep the cells approximately isotropic near the grid centerline. The grid is slowly stretched with respect to axial and radial spacing from zero to 30 jet exit diameters downstream from the jet exit, and then coarsened more rapidly in axial spacing from 30 to 36.67 diameters downstream. The four grids are summarized as follows:

- Grid 120: Circumferential spacing = 3.0 degrees, total size = 4.43M hexahedral cells.
- Grid 180: Circumferential spacing = 2.0 degrees, total size = 13.8M hexahedral cells.
- Grid 240: Circumferential spacing = 1.5 degrees, total size = 31.5M hexahedral cells.
- Grid 360: Circumferential spacing = 1.0 degrees, total size = 101M hexahedral cells.

Total pressure and temperature conditions (from Refs. 12 and 13) were prescribed at the nozzle inflow boundary. Viscous no-slip walls (with a fixed wall temperature of 278 K) were prescribed on the nozzle interior wall surfaces, and the short section of wall proceeding upstream from the nozzle exit to the larger domain upstream boundary. A characteristic-based boundary condition ($P = 101325$ Pa, $T = 278$ K and $M = 0.01$) was used at the upstream and radial farfield boundaries. A zeroth-order extrapolation boundary was prescribed for the downstream farfield boundary. Time integration was accomplished by a second-order implicit backward-differentiation method, using a timestep set by a convective Courant-Friedrichs-Lewy (CFL) number near unity for cells in the near field of the jet exit.

A sample of the LES results will be outlined briefly. The emphasis in this particular work is primarily on the characteristics of various inviscid flux numerical discretizations and methods on this problem, rather than the coupling of various schemes with LES subgrid-scale (SGS) turbulence models. As such, no explicit SGS models are included in the calculations. Typical snapshots of the LES flowfield for the supersonic hot jet case on grid 180 are shown in figures 1, 2 and 3. In these figures, an isosurface of the Q -criterion, $Q = (\mathbf{R} : \mathbf{R} - \mathbf{S} : \mathbf{S})/2$ is displayed, where \mathbf{R} is the rotation-rate tensor $(\nabla \mathbf{u} - \nabla \mathbf{u}^T)/2$, and \mathbf{S} is the strain-rate tensor $(\nabla \mathbf{u} + \nabla \mathbf{u}^T)/2$ (\mathbf{u} is the velocity vector, $[u, v, w]^T$). The isosurface of $Q = 0.01 (u_{\text{jet exit}}/D)^2$ is shown colored by Mach number M in the upper part of each figure. Contours of $Q(D/u_{\text{jet exit}})^2$ and Mach number M at a distance of $18D$ downstream of the jet exit are shown in the lower part of the figures. It is evident from these figures that the low dissipation scheme LDS4 (figure 1) resolves finer turbulent structures than the OGRE-Roe scheme (figure 2), and particularly the LS-Roe scheme (figure 3).

The LES simulations were initialized using a RANS solution. For the cold jet case, the simulations were run for 80 ms to wash out the flow transition to LES flow, and then for another 80 ms to collect turbulence statistics. 80 ms corresponds to 469 timescales of $D/u_{\text{jet exit}}$ for the cold jet case. For the hot jet case, two corresponding time intervals of 40 ms were used, each equivalent to 443 timescales of $D/u_{\text{jet exit}}$. Comparisons of the time-averaged centerline Mach number, normalized total temperature ($T_t/T_{t,\text{jet exit}}$), and normalized total pressure ($P_t/P_{t,\text{jet exit}}$) from the LES simulations with experimental data are shown in figures 4, 5 and 6 respectively. Observe that the LDS4 scheme generally produces quite good agreement with the experimental data on Grids 240 and 360, and often for Grid 180 as well. The length of the inviscid core and the decay rate after the end of the core are well-predicted by the LES results. The OGRE-Roe scheme yields steadily improving agreement with the data with increased grid resolution. The OGRE-Roe results shown for Grid 360 are preliminary at the time of this writing, but already appear to be in good agreement with the data. The LS-Roe scheme produces results which tend to underpredict the inviscid core length, or which predict a faster rate of decay, or both.

Similar observations hold with axial comparisons of space- and time-averaged values of the jet half-velocity radius, $R_{0.5}$ and the mixing layer half-velocity thickness, $b = R_{0.5} - h$, where h is the potential core radius (which is set to zero after the end of the core). Comparisons of these values, normalized by the jet exit radius, $R = D/2$, are shown for all three numerical schemes in figures 7 and 8, respectively. The jet half-velocity radius $R_{0.5}$ is straightforward to compute from the space- and time-averaged velocity results. the potential core radius h is determined by examining the radial profile of the space- and time-averaged total pressure at a given axial station. As above, the LDS4 scheme yields the best agreement with the experimental data, particularly on Grids 240 and 360.

The final paper will explain the fourth-order low-dissipation scheme, the computational domain, the grid structure, and the boundary conditions in more detail. The initialization, time-integration, and the time- and space-averaging procedures will be described. It will include an evaluation of timestep sensitivity and turbulence spectra. Comparisons of LES simulations of the hot jet case with near-field acoustic measurements from Ref. 11 will be included. A summary of RANS results on axisymmetric versions of the above grids will also be included.

References

- ¹Moin, P., "Numerical and Physical Issues in Large Eddy Simulation of Turbulent Flows," *JSME International Journal, Series B*, Vol. 41, No. 2, 1998, pp. 454 – 463.
- ²Fureby, C., "Towards the use of large eddy simulation in engineering," *Progress in Aerospace Sciences*, Vol. 44, No. 6, 2008, pp. 381 – 396.
- ³Georgiadis, N. J., Rizzetta, D. P., and Fureby, C., "Large-Eddy Simulation: Current Capabilities, Recommended Practices, and Future Research," *AIAA Journal*, Vol. 48, No. 8, 2010, pp. 1772 – 1784.
- ⁴Spalart, P. R., Jou, W.-H., Strelets, M., and Allmaras, S. R., "Comments on the feasibility of LES for wings, and on a hybrid RANS/LES approach," In "Advances in DNS/LES: proceedings of the First AFOSR International Conference on DNS/LES", C. Liu and Z. Liu Eds., Greyden Press, Columbus, OH.
- ⁵Bodony, D. J. and Lele, S. K., "Current Status of Jet Noise Predictions Using Large-Eddy Simulation," *AIAA Journal*, Vol. 46, No. 2, 2008, pp. 364–380.
- ⁶Liu, J., Kailasanath, K., Ramamurti, R., Munday, D., Gutmark, E., and Lohner, R., "Large-Eddy Simulations of a Supersonic Jet and Its Near-Field Acoustic Properties," *AIAA Journal*, Vol. 47, No. 8, 2009, pp. 1849–1865.
- ⁷DeBonis, J., "A High-Resolution Capability for Large-Eddy Simulation of Jet Flows," AIAA Paper 2010-5023, June 2010.
- ⁸Khalighi, Y., Ham, F., Nichols, J., Lele, S., and Moin, P., "Unstructured Large Eddy Simulation for Prediction of Noise Issued from Turbulent Jets in Various Configurations," AIAA Paper 2011-2886, June 2011.

- ⁹Brès, G., Nichols, J., Lele, S., and Ham, F., “Towards Best Practices for Jet Noise Predictions with Unstructured Large Eddy Simulations,” AIAA Paper 2012-2965, June 2012.
- ¹⁰Viswanath, K., Johnson, R., Corrigan, A., Kailasanath, K., Mora, P., Baier, F., and Gutmark, E., “Flow Statistics and Noise of Ideally Expanded Supersonic Rectangular and Circular Jets,” *AIAA Journal*, Vol. 55, No. 10, 2017, pp. 3425–3439.
- ¹¹Seiner, J. M., Ponton, M. K., Jansen, B. J., and Lagen, N. T., “The Effects of Temperature on Supersonic Jet Noise Emission,” AIAA Paper 1992-02-046, May 1992.
- ¹²Rumsey, C., “NASA Langley Turbulence Modeling Resource, ACSSJ: Axisymmetric Cold Supersonic Jet,” https://turbmodels.larc.nasa.gov/jetsupersoniccold_val.html.
- ¹³Rumsey, C., “NASA Langley Turbulence Modeling Resource, AHSSJ: Axisymmetric Hot Supersonic Jet,” https://turbmodels.larc.nasa.gov/jetsupersonichot_val.html.
- ¹⁴Luke, E. A., Tong, X., Wu, J., Tang, L., and Cinnella, P., “A Step Towards ‘Shape-Shifting’ Algorithms: Reacting Flow Simulations Using Generalized Grids,” AIAA Paper 2001-0897, Jan. 2001.
- ¹⁵Luke, E. A., *A Rule-Based Specification System for Computational Fluid Dynamics*, Ph.D. thesis, Mississippi State University, Mississippi, 1999.
- ¹⁶Barth, T. J. and Jespersen, D. C., “The Design and Application of Upwind Schemes on Unstructured Meshes,” AIAA Paper 1989-0366, Jan. 1989.
- ¹⁷Venkatakrishnan, V., “On the Accuracy of Limiters and Convergence to Steady State Solutions,” AIAA Paper 1993-0880, Jan. 1993.
- ¹⁸Roe, P. L., “Approximate Riemann solvers, parameter vectors, and difference schemes,” *Journal of Computational Physics*, Vol. 43, No. 2, 1981, pp. 357 – 372.
- ¹⁹Poe, N. M. W., Walters, D. K., Luke, E. A., and Morris, C. I., “A Low-Dissipation Second-Order Upwind Flux Formulation for Simulation of Complex Turbulent Flows,” *ASME International Mechanical Engineering Congress and Exposition, Volume 7A: Fluids Engineering Systems and Technologies*, 2015.
- ²⁰Thornber, B., Drikakis, D., Williams, R., and Youngs, D., “On entropy generation and dissipation of kinetic energy in high-resolution shock-capturing schemes,” *Journal of Computational Physics*, Vol. 227, No. 10, 2008, pp. 4853 – 4872.
- ²¹Thornber, B., Mosedale, A., Drikakis, D., Youngs, D., and Williams, R., “An improved reconstruction method for compressible flows with low Mach number features,” *Journal of Computational Physics*, Vol. 227, No. 10, 2008, pp. 4873 – 4894.

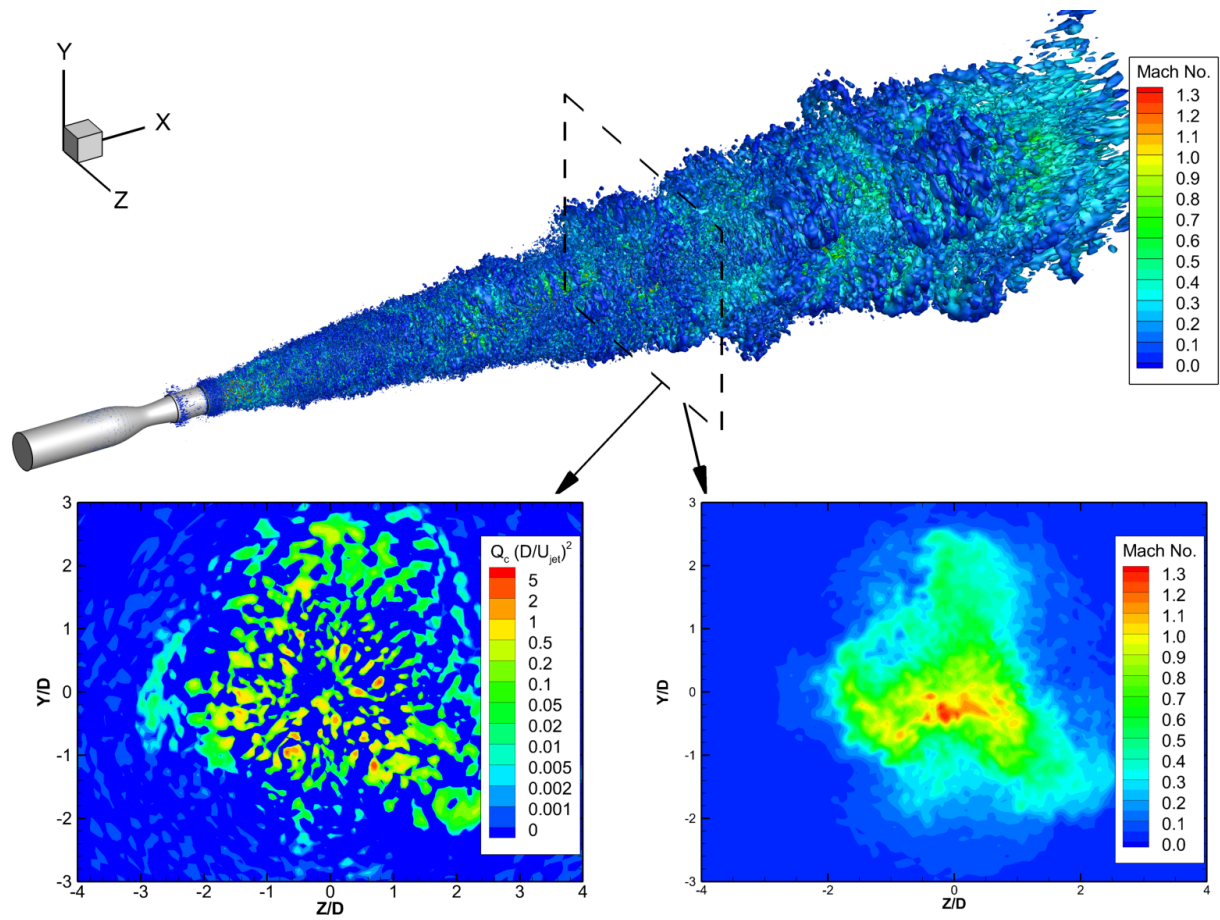


Figure 1. Plot illustrating hot jet structure on Grid 180. The isosurface of $Q = 0.01 (u_{jet_exit}/D)^2$ is shown colored by Mach number M in the upper part of the figure. Contours of $Q(D/u_{jet_exit})^2$ and Mach number M at a distance of $18D$ downstream of the jet exit are shown in the lower part of the figure. Inviscid flux: LDS4.

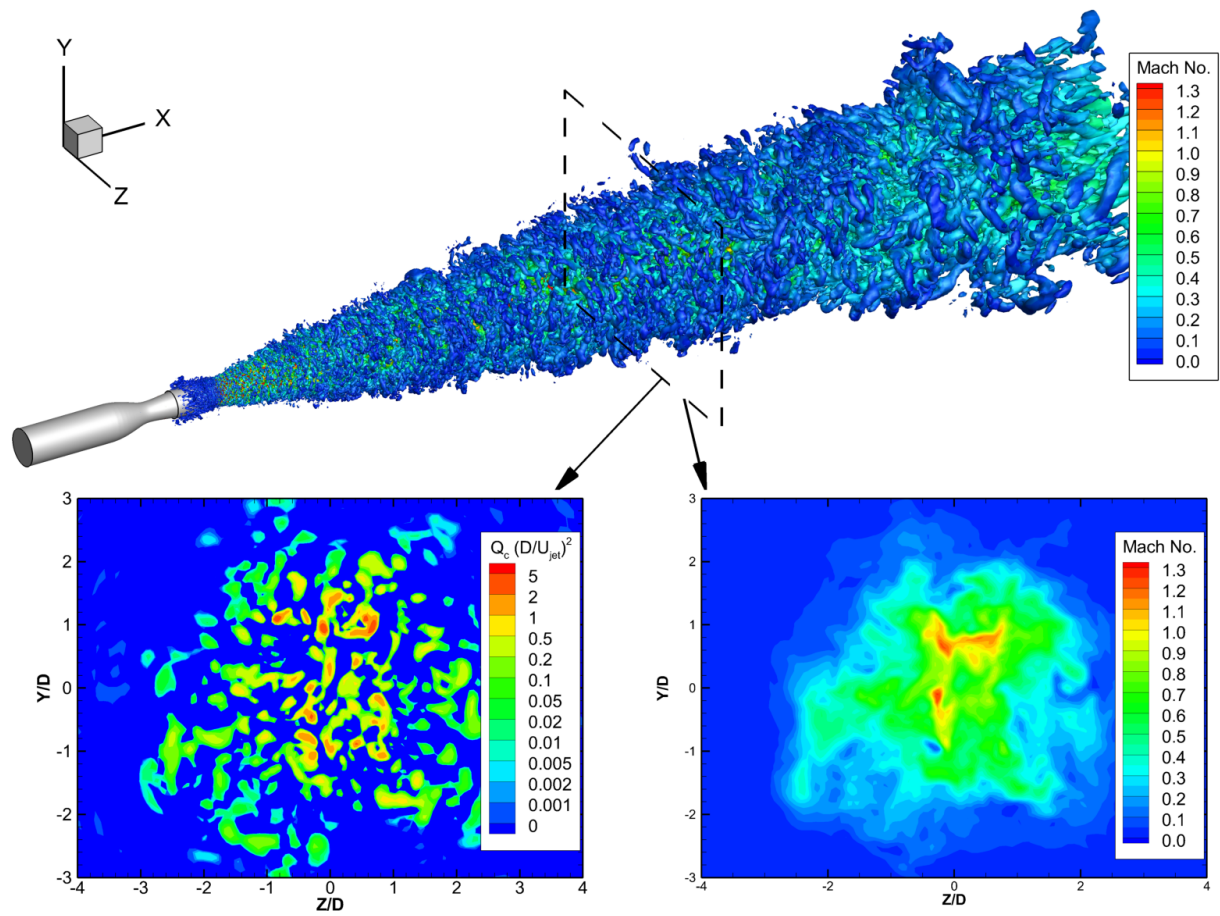


Figure 2. Plot illustrating hot jet structure on Grid 180. The isosurface of $Q = 0.01 (u_{jet_exit}/D)^2$ is shown colored by Mach number M in the upper part of the figure. Contours of $Q(D/u_{jet_exit})^2$ and Mach number M at a distance of $18D$ downstream of the jet exit are shown in the lower part of the figure. Inviscid flux: OGRE-Roe.

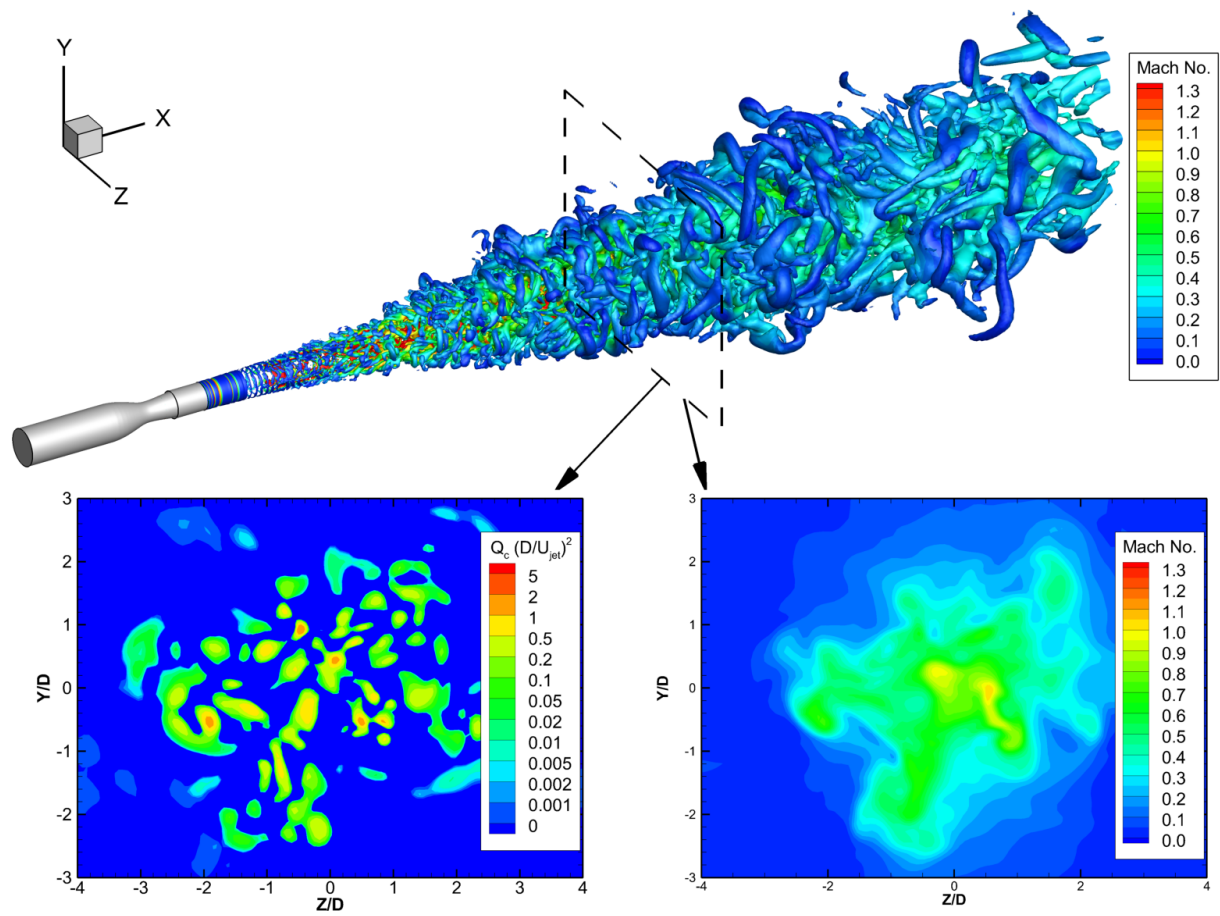
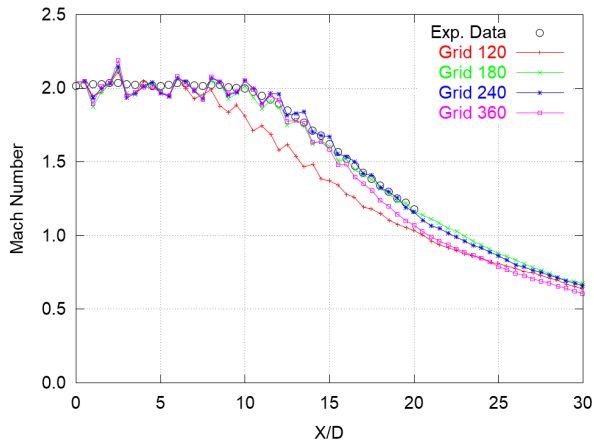
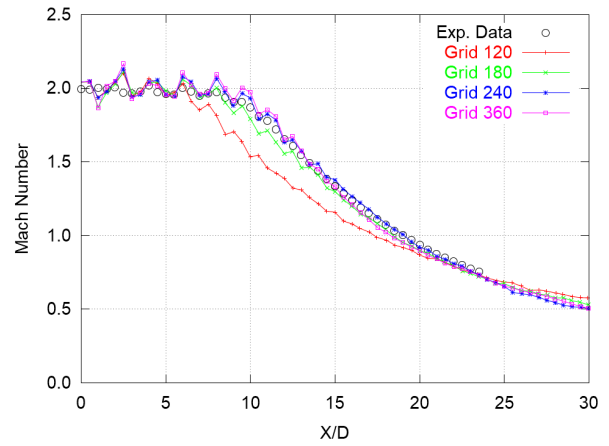


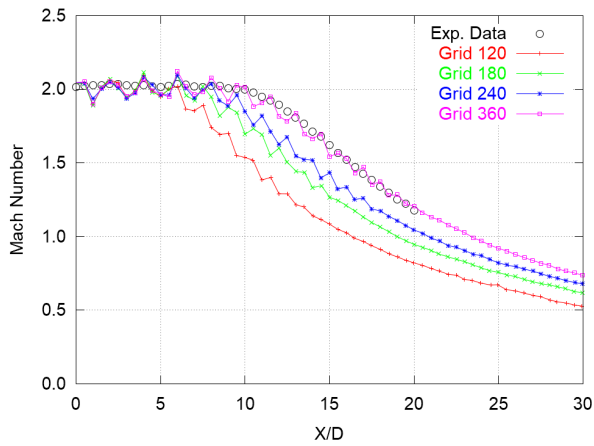
Figure 3. Plot illustrating hot jet structure on Grid 180. The isosurface of $Q = 0.01 (u_{jet_exit}/D)^2$ is shown colored by Mach number M in the upper part of the figure. Contours of $Q(D/u_{jet_exit})^2$ and Mach number M at a distance of $18D$ downstream of the jet exit are shown in the lower part of the figure. Inviscid flux: LS-Roe.



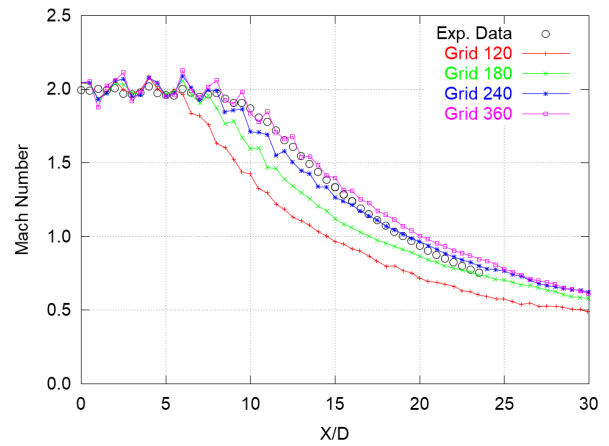
(a) Cold Jet - LDS4



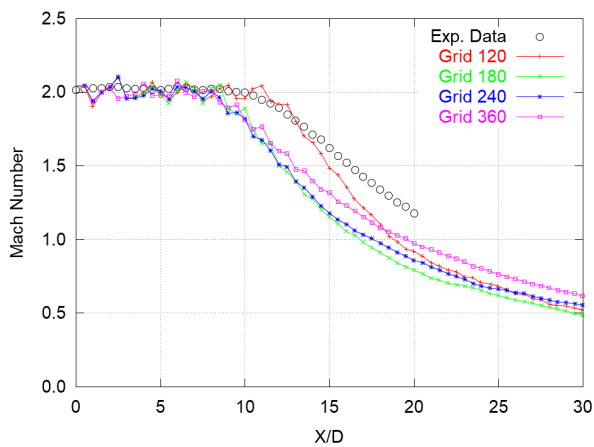
(b) Hot Jet - LDS4



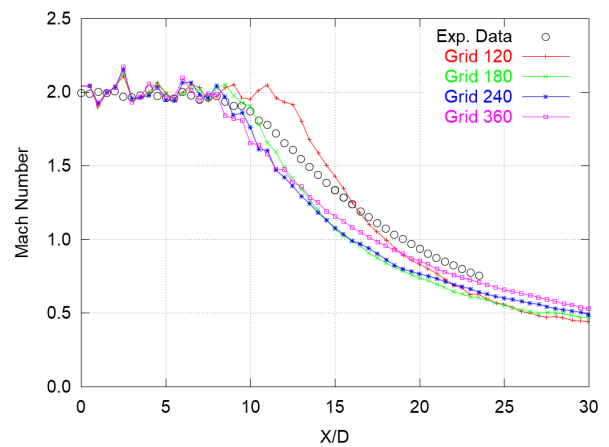
(c) Cold Jet - OGRE-Roe



(d) Hot Jet - OGRE-Roe

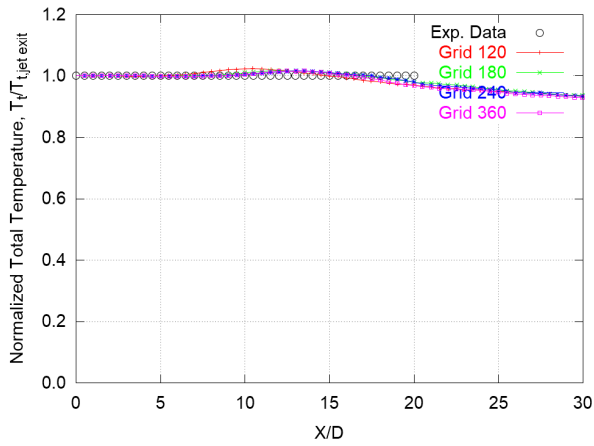


(e) Cold Jet - LS-Roe

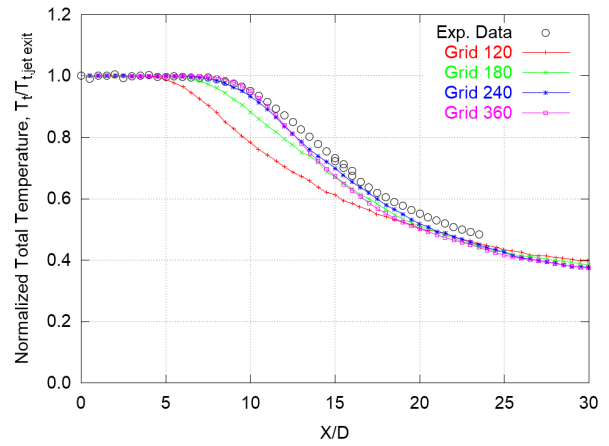


(f) Hot Jet - LS-Roe

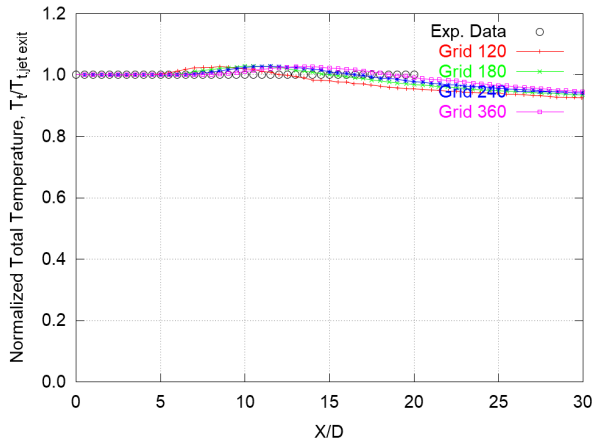
Figure 4. Effect of grid resolution on the time-averaged Mach number on the jet axial centerline. Left panel: cold jet case. Right panel: hot jet case.



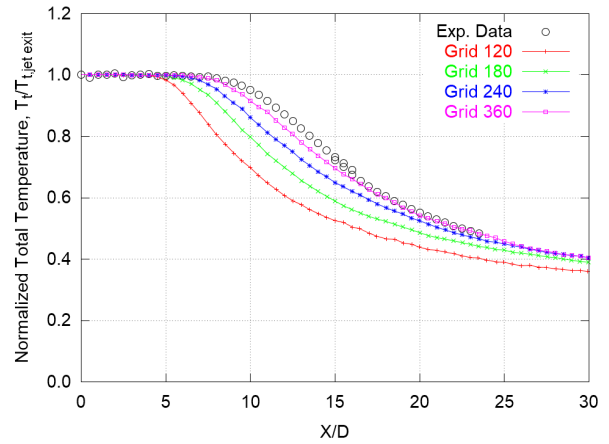
(a) Cold Jet - LDS4



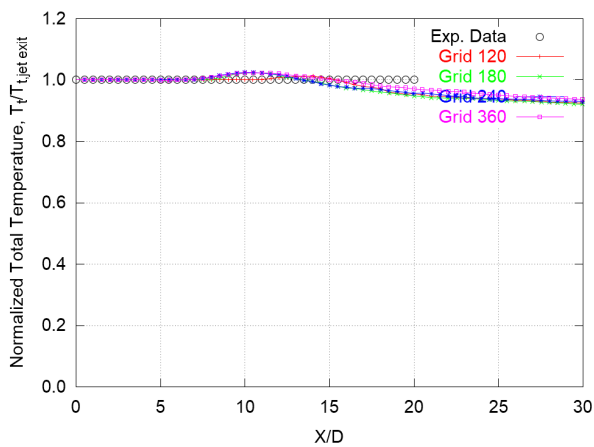
(b) Hot Jet - LDS4



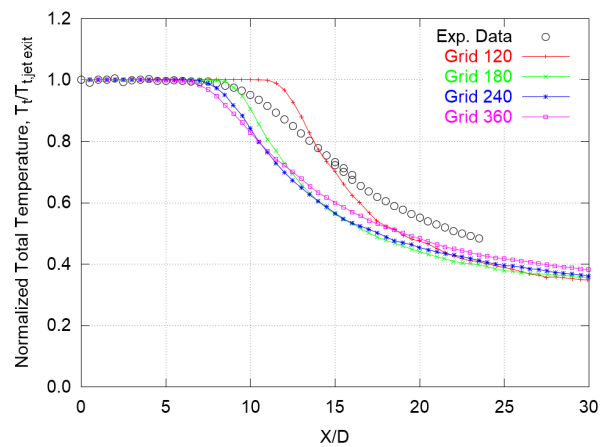
(c) Cold Jet - OGRE-Roe



(d) Hot Jet - OGRE-Roe

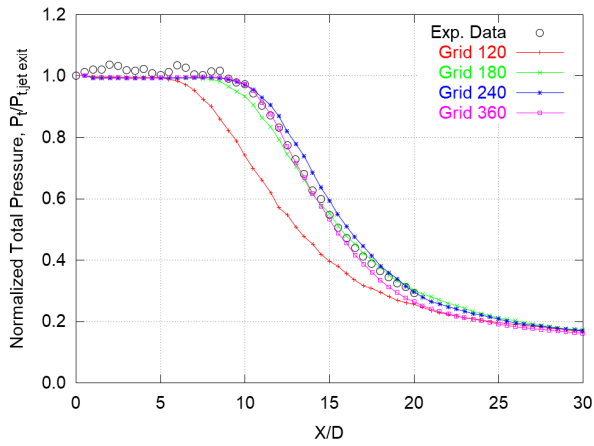


(e) Cold Jet - LS-Roe

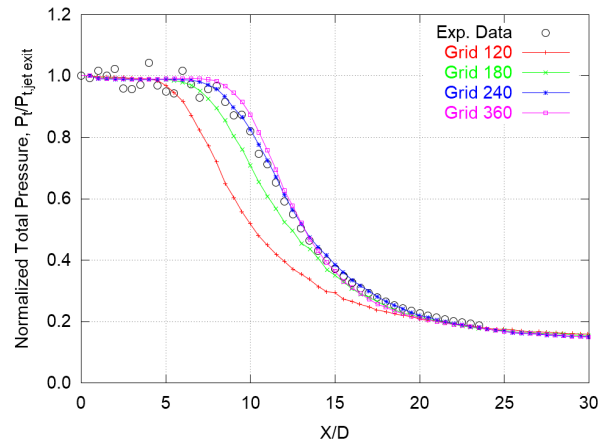


(f) Hot Jet - LS-Roe

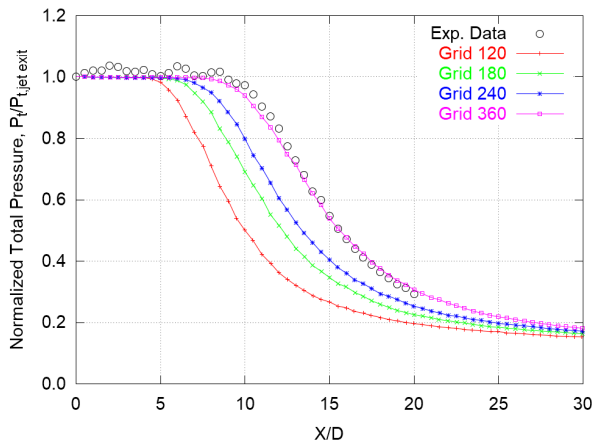
Figure 5. Effect of grid resolution on the time-averaged total temperature on the jet axial centerline. Left panel: cold jet case. Right panel: hot jet case.



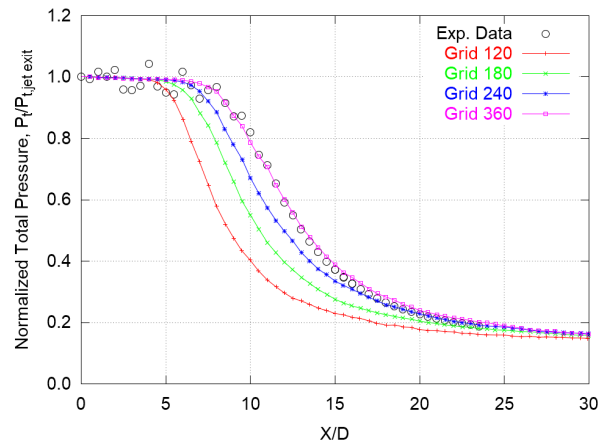
(a) Cold Jet - LDS4



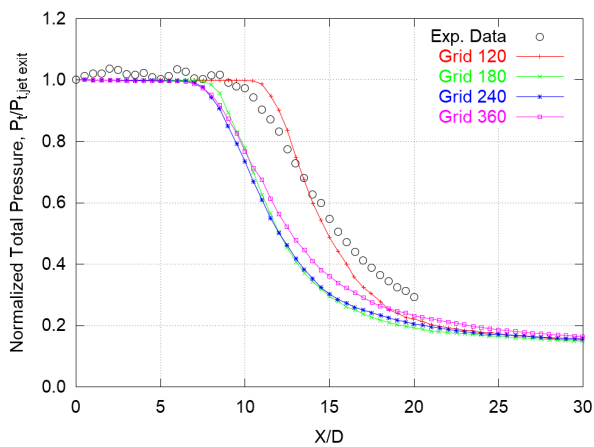
(b) Hot Jet - LDS4



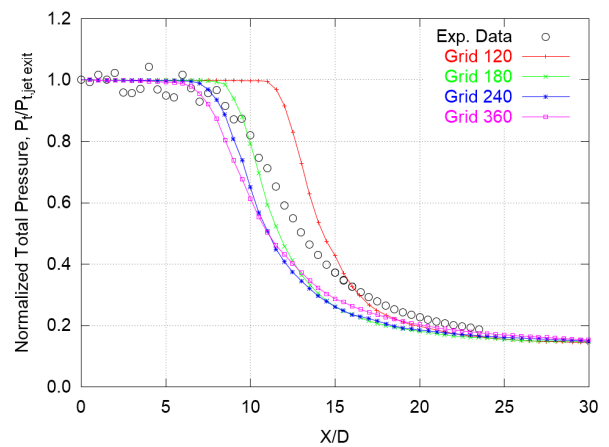
(c) Cold Jet - OGRE-Roe



(d) Hot Jet - OGRE-Roe

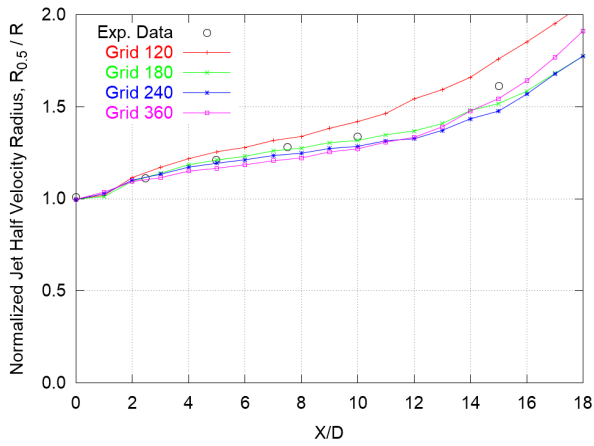


(e) Cold Jet - LS-Roe

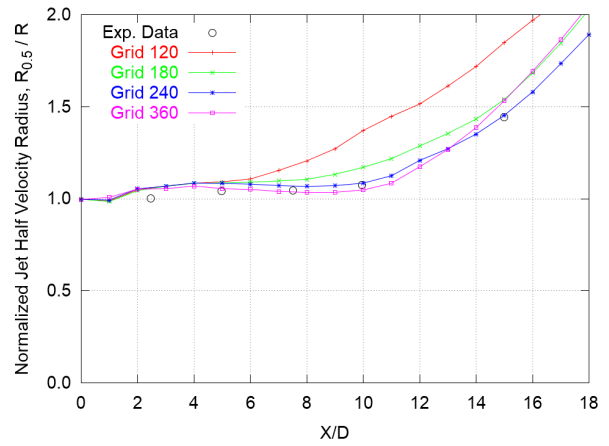


(f) Hot Jet - LS-Roe

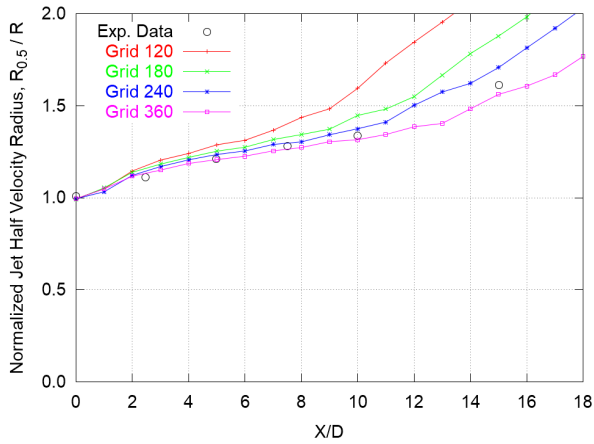
Figure 6. Effect of grid resolution on the time-averaged total pressure on the jet axial centerline. Left panel: cold jet case. Right panel: hot jet case.



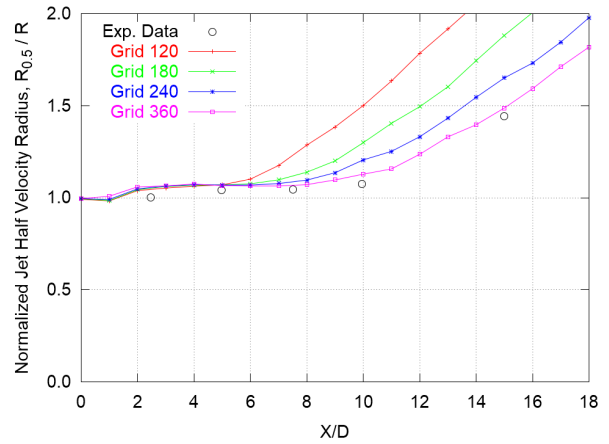
(a) Cold Jet - LDS4



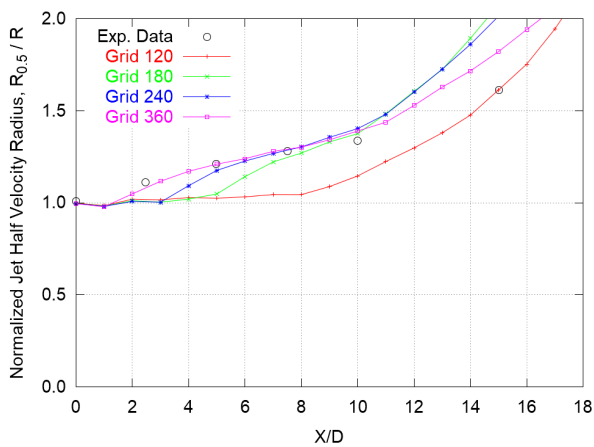
(b) Hot Jet - LDS4



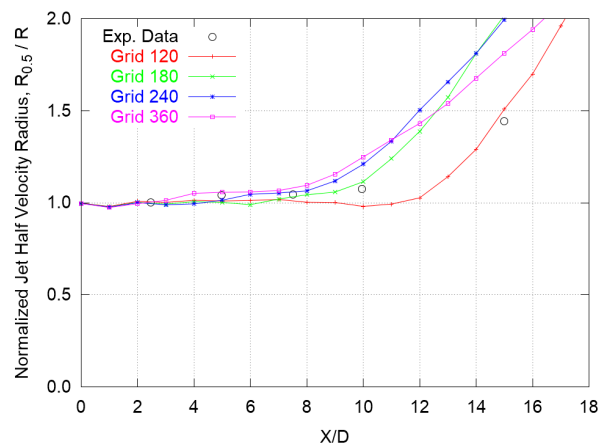
(c) Cold Jet - OGRE-Roe



(d) Hot Jet - OGRE-Roe

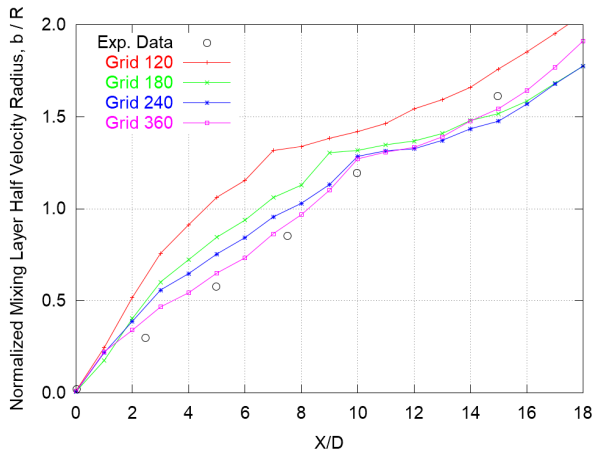


(e) Cold Jet - LS-Roe

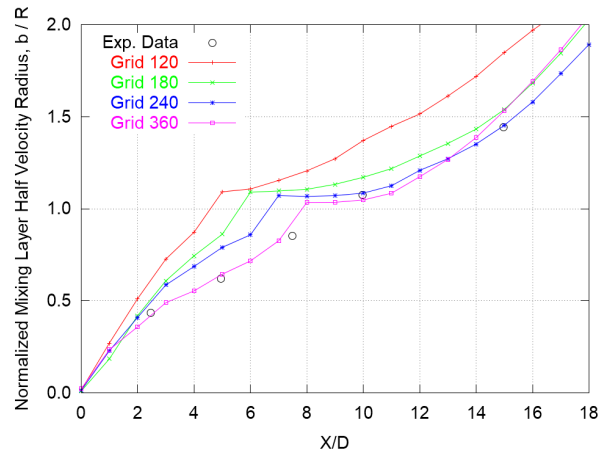


(f) Hot Jet - LS-Roe

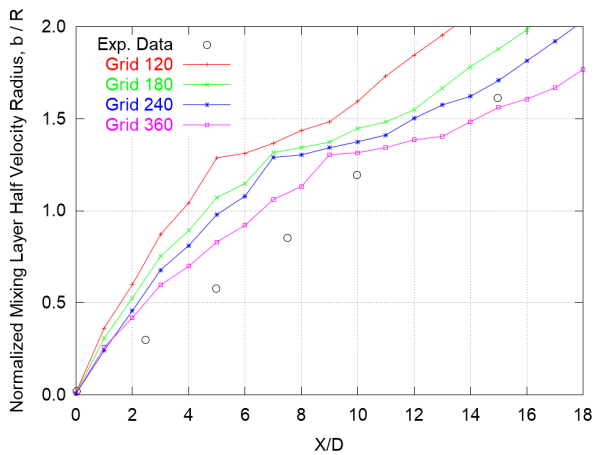
Figure 7. Effect of grid resolution on the space- and time-averaged jet half velocity radius. Left panel: cold jet case. Right panel: hot jet case.



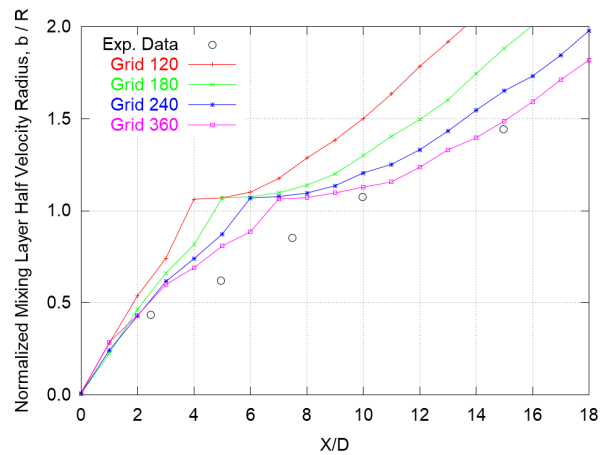
(a) Cold Jet - LDS4



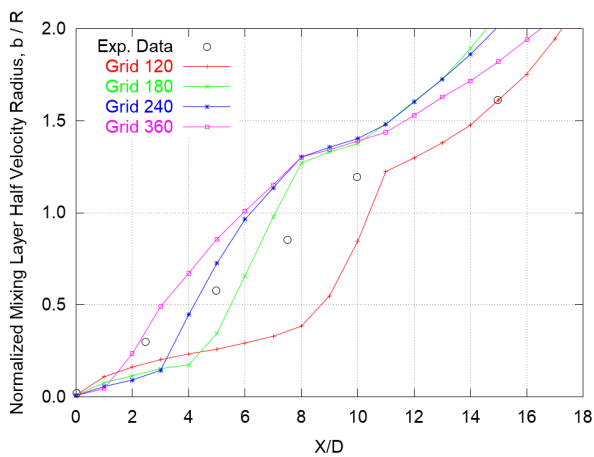
(b) Hot Jet - LDS4



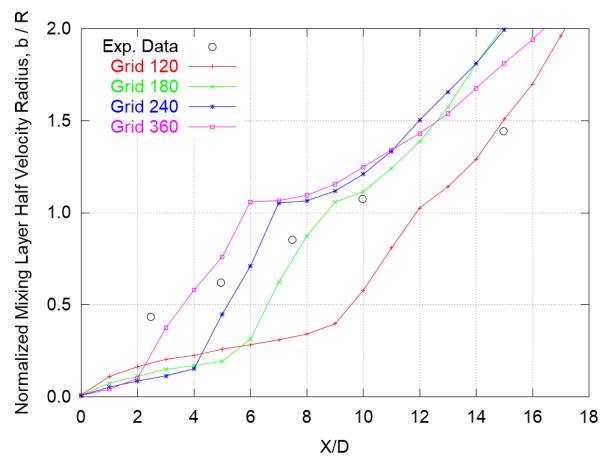
(c) Cold Jet - OGRE-Roe



(d) Hot Jet - OGRE-Roe



(e) Cold Jet - LS-Roe



(f) Hot Jet - LS-Roe

Figure 8. Effect of grid resolution on the space- and time-averaged mixing layer half velocity radius. Left panel: cold jet case. Right panel: hot jet case.